Exploring zinc oxide morphologies for aqueous solar cells by a photoelectrochemical, computational, and multivariate approach

Energy Advances

ROYAL SOCIETY OF CHEMISTRY

PAPER

View Article Online
View Journal | View Issue

Cite this: *Energy Adv.*, 2024, 3, 1062

Exploring zinc oxide morphologies for aqueous solar cells by a photoelectrochemical, computational, and multivariate approach†

Elisa Maruccia,[a] Simone Galliano,[b] Eduardo Schiavo,[c] Nadia Garino,[a] Ana Y. Segura Zarate,[bd] Ana B. Muñoz-García,[e] Michele Pavone,[c] Claudio Gerbaldi,[a] Claudia Barolo,[bfg] Valentina Cauda[a] and Federico Bella*[a]

Received 4th January 2024,
Accepted 26th April 2024

DOI: 10.1039/d4ya00010b

rsc.li/energy-advances

Dye-sensitized solar cells assembled with aqueous electrolytes are emerging as a sustainable photovoltaic technology suitable for safe indoor and portable electronics use. While the scientific community is exploring unconventional materials for preparing electrodes and electrolytes, this work presents the first study on zinc oxide as a semiconductor material to fabricate photoanodes for aqueous solar cells. Different morphologies (*i.e.*, nanoparticles, multipods, and desert roses) are synthesized, characterized, and tested in laboratory-scale prototypes. This exploratory work, also integrated by a computational study and a multivariate investigation on the factors that influence electrode sensitization, confirms the possibility of using zinc oxide in the field of aqueous photovoltaics and opens the way to new morphologies and processes of functionalization or surface activation to boost the overall cell efficiency.

Introduction

The energy transition, the primary objective of safeguarding the planet, dominates the international scenario where the scientific community operates.[1–5] The pillars of the current work plan are the ability to produce and store energy through renewable sources, sustainable technologies, and the minimization of environmental emissions.[6–10] In this context, photovoltaics continues to excel for its well-known advantages, first and foremost the abundance and geographically non-polarized distribution of its source.[11–15]

Although silicon-based photovoltaic technology has seen, in the last twenty years, a continuous lowering of production costs,[16] the scientific community's attention has also been focused on new technologies capable of providing better aspects.[17–21] Among these characteristics, the use of materials that require production and manufacturing processes carried out in mild conditions, the ability of solar cells to work even indoors or in a vertical position, and the possibility of manufacturing flexible devices have emerged and have led to new classes of photovoltaic cells, such as perovskite solar cells[22–26] and dye-sensitized solar cells (DSSCs).[27–31] While the formers have achieved and exceeded the performance of silicon-based photovoltaics, with which they can also be combined in tandem devices,[32–34] the DSSCs have unique properties in terms of transparency, variety of available colors, absence of heavy metals in their active components.[35–39]

One of the topics currently active in the field of DSSCs concerns the replacement of the organic solvents used for the formulation of the liquid electrolyte with water.[40,41] This would represent an evident product sustainability and safety advantage given the integration of DSSCs with portable devices; also, water would lead to better solvent properties towards more redox couples and additives, as well as greater durability due to reduced electrolyte evaporation.[42,43] This prompted researchers to develop materials for the so-called aqueous DSSCs, proposing new formulations of liquid and gel-polymer

[a] *Department of Applied Science and Technology, Politecnico di Torino, Corso Duca degli Abruzzi 24, 10129 – Torino, Italy. E-mail: federico.bella@polito.it*
[b] *Department of Chemistry, NIS Interdepartmental Centre and INSTM Reference Centre, Università degli Studi di Torino, Via Pietro Giuria 7, 10125 – Torino, Italy*
[c] *Department of Chemical Sciences, Università di Napoli Federico II, Comp. Univ. Monte Sant'Angelo, Via Cintia 21, 80126 – Napoli, Italy*
[d] *Escuela de Física, Instituto Tecnológico de Costa Rica, TEC, 159-7050 – Cartago, Costa Rica*
[e] *Department of Physics "Ettore Pancini", Università di Napoli Federico II, Comp. Univ. Monte Sant'Angelo, Via Cintia 21, 80126 – Napoli, Italy*
[f] *ICxT Interdepartmental Centre, Università degli Studi di Torino, Via Lungo Dora Siena 100, 10153 – Torino, Italy*
[g] *Istituto di Scienza, Tecnologia e Sostenibilità per lo Sviluppo dei Materiali Ceramici (ISSMC-CNR), Via Granarolo 64, 48018 – Faenza, Italy*

† Electronic supplementary information (ESI) available. See DOI: https://doi.org/10.1039/d4ya00010b

electrolytes,[44–47] aqueous stable dyes,[48–50] photoanode treatment protocols,[51–53] platinum-free counter electrodes[54,55] to further reduce the cost and impact of this technology. In these first years of research activity, maximum photovoltaic performances of the order of 6–7% have been achieved[56,57] and further experimental and computational investigations are currently underway to try to reduce the efficiency gap with respect to the corresponding DSSCs manufactured with nitriles-based organic solvents.

ZnO represents one of the closest alternatives to TiO_2 as a photoanode active material in DSSCs. Indeed, these two semiconductors show almost the same electron affinities and band-gap energies (*i.e.*, ≈3.2 and ≈3.3 eV), are available at low cost, and remain stable to photo-corrosion. Moreover, ZnO offers essential features for photovoltaic applications, that can be resumed as follows: (i) a much higher electron diffusivity than TiO_2; (ii) a high electron mobility (*i.e.*, 115–155 $cm^2\ V^{-1}\ s^{-1}$); (iii) a significant excitation binding energy (60 eV); (iv) a crystalline structure conducting to anisotropic growth, making readily available a comprehensive list of diverse morphologies.[58–60] ZnO-based DSSCs have thus been well explored in the previous years by the scientific community, with excellent outcomes also attributed to the efficient electron transport of this semiconductor and the resulting reduced recombination reactions in the photoelectrochemical cell.[61,62]

Despite the exciting aspects described above for ZnO-based photoanodes, no articles have yet been published with this electrode combined with an aqueous electrolyte in DSSCs. Therefore, this work focuses on aqueous DSSCs fabricated with three different ZnO electrodes synthesized in our group and characterized by various morphological, dimensional, and surface aspects. Besides dealing with materials synthesis and photovoltaic cell fabrication and characterization, our activity was also aided by a computational study and a multivariate chemometric analysis to better investigate both the interaction of ZnO with the molecular dye chosen for this work and the best experimental conditions to carry out electrode sensitization.

Materials and methods

ZnO micro- and nanostructures: synthesis and characterization

ZnO microparticles were synthesized through a shape-controlled hydrothermal process, combining zinc nitrate hexahydrate ($Zn(NO_3)_2{\cdot}6H_2O$, 99%, Sigma-Aldrich) and potassium hydroxide (KOH, 85%, Sigma-Aldrich). The desert rose (DR) and the multipod (MP) morphologies were obtained by varying the $KOH : Zn(NO_3)_2$ molar ratio from 2 to 8, respectively. More in detail, two separated solutions were prepared by dissolving 14.8 g of $Zn(NO_3)_2{\cdot}6H_2O$ in 100 mL of bidistilled water (Milli-Q® water, 18 MΩ cm at 25 °C, obtained with a Direct-Q® 3 UV purification system by Merck Millipore), and the corresponding amount of KOH in the same water volume. Then, a $Zn(NO_3)_2{\cdot}6H_2O$ solution was drop-wise added to the KOH one by vigorously stirring. The gel was kept in a closed Teflon bottle at 70 °C for 4 h; the desired ZnO microstructures were formed later. Finally, the microparticles were separated from the reaction medium by repeated rinsing and filtration with deionized water until the pH was neutralized. The powders were finally dried in air at 60 °C overnight.

ZnO nanoparticles (NPs) were prepared by following a microwave-assisted solvothermal route by combining, directly in the Teflon reactor vessel, 60 mL of a methanol (Reag. Ph. Eur. Grade, VWR Chemicals) 0.09 M solution of zinc acetate dihydrate ($Zn(CH_3COO)_2{\cdot}2H_2O$, ACS reagent, ≥98%, Sigma-Aldrich) with 480 μL of double-distilled water, and a potassium hydroxide solution (0.2 M in methanol, 35 mL, KOH ≥85% pellets, Sigma-Aldrich). The reactor was equipped with pressure and temperature probes and connected to the microwave furnace (Milestone START-Synth, Milestone Inc.). The chemical precursor solution was heated at 60 °C for 30 min and then cooled to room temperature. The resulting NPs dispersion was then collected and centrifuged for 10 min at 3500 g (Mega Star 600R, VWR); then, the supernatant was removed, the residue was dispersed and washed twice in 15 mL of ethanol (Sigma-Aldrich, 99%) to release any unreacted compound. Finally, the powders were dried in air at room temperature.

The crystallinity grade of the different ZnO structures was analysed by X-rays diffraction (XRD) on a Panalytical's X'Pert[3] MRD PRO diffractometer with Cu-Kα X-rays radiation source ($\lambda \approx 1.54$ Å) in θ–2θ Bragg–Brentano configuration (2θ angle range between 20° and 60°). The morphology investigation and the dimensional measurements were carried out by a field emission scanning electron microscope (FESEM, Dual Beam Auriga from Carl Zeiss, operating at 5 keV). The Branauer–Emmett–Teller (BET) specific surface area was estimated from N_2 desorption isotherms at 77 K by a Micromeritics ASAP 2020 Plus Physisorption facility. An estimation of the dye loading capacity for the different ZnO microstructures was performed by comparing the residual concentrations of the dye in the sensitizing solutions using a Cary 5000 UV-Vis-NIR spectrophotometer by Agilent Technologies, Inc.

DSSCs: fabrication and characterization of lab-scale prototypes

ZnO particles were dispersed in a solution consisting of 66 vol% ethanol (≥99.9%, Carlo Erba Reagents), 33 vol% bidistilled water, and 1 vol% acetic acid (≥99.9%, Sigma-Aldrich), in a weight ratio of 1 : 2 between the powder and the solution. The dispersion was then homogenized in an ultrasonic bath (Elmasonic P, Elma Schmidbauer GmbH) at 80 kHz for 4 h. A square-shaped spot of ZnO paste was deposited with an area of 0.25 cm^2 onto a fluorine-doped SnO_2 (FTO)-coated glass by using the doctor blading technique. The FTO substrate (thickness 2.2 mm, resistivity 7 Ω sq^{-1}, Solaronix SA) was previously cleaned, in three subsequent steps, by using bidistilled soapy water, acetone (≥99%, Honeywell), and ethanol (≥99.8%, Honeywell), to remove any contamination. ZnO paste-coated glass underwent a thermal treatment of drying at 90 °C for 30 min and sintering at 450 °C for 10 min in air. When the electrodes were cooled down at about 70 °C, they were soaked in a sensitizing solution of the dye, *i.e.*, 2-[{4-[4-(2,2-diphenylethenyl)phenyl]-1,2,3,3*a*,4,8*b*-hexahydrocyclopento[*b*]indole-7-yl}methylidene] cyanoacetic acid (D131),

purchased from Inabata Europe SA; the electrodes were finally rinsed in acetone to remove the dye molecules which were not adsorbed. The composition of the sensitization solution was properly investigated in our experimental work; in particular, the optimal molar ratio between the co-adsorbent, *i.e.*, chenodeoxycholic acid (CDCA, ≥97%, Sigma-Aldrich), and the dye was evaluated through a chemometric approach (see next section). D131 dye was chosen for this work since it is the sensitizer that our group has widely explored in previous research activities (*e.g.* ref. 53) and that has passed our reproducibility and stability tests.

A fully aqueous quasi-solid electrolyte was prepared using the I^-/I_3^- redox couple. In detail, the electrolyte solution was obtained by dissolving NaI 3.0 M (≥99.0%, Sigma-Aldrich) and I_2 20 mM (≥99.8%, Sigma-Aldrich) in deionized water saturated with CDCA. Sodium carboxymethyl cellulose (Na-CMC, M_w = 250 000 g mol^{-1}, Sigma-Aldrich) was chosen as a bio-sourced jellifying agent and added (3 wt%) to the liquid solution; the quasi-solid consistency was achieved after stirring for about 2 h at 40 °C.

The counter-electrodes were prepared by a two-step deposition process, carrying out the thermal decomposition of a platinum catalyst precursor, *i.e.*, a H_2PtCl_6 5 mM ethanol solution (Sigma-Aldrich), at 450 °C for 30 min.

As regards lab-scale prototype fabrication, 1.6–1.7 mg of quasi-solid electrolyte were deposited on the photoanode; then, it was faced to the counter-electrode using a Meltonix 1170-60 thermoplastic film (Solaronix SA) as both spacer and sealant; the cell was subsequently hot pressed at 90 °C for 15 s.

The photovoltaic characterization (*J*–*V* measurements) was carried out by a source measure unit (model 2440, Keithley) and a sun simulator under AM1.5G irradiation with a power output of 100 mW cm^{-2}, calibrated by a silicon reference solar cell. DSSCs performances were assessed through short-circuit current density (J_{sc}), open-circuit voltage (V_{oc}), fill factor (FF), and power conversion efficiency (PCE) figures of merit. Electrochemical impedance spectroscopy (EIS) was performed under dark conditions using a potentiostat (Biologic, VMP-3) in the frequency range between 100 kHz and 0.1 Hz. A potential equal to the V_{oc} (previously measured under standard illumination conditions) was overlapped with the AC signal of 10 mV of amplitude. The EC-Lab V11-18 software was used to fit the EIS data.

Design of experiments

The investigation of the newly proposed ZnO electrodes for aqueous DSSCs was guided by a design of experiment (DoE) approach, with the aid of the software MODDE (version 11.0.2.2309, Umetrics). Of note, DoE is an experimental strategy that maximizes the quantity and quality of information resulting from a minimum number of trials. In this work, DoE was adopted to find the optimal sensitizing conditions for ZnO photoanodes to (i) obtain the best photovoltaic performances, and (ii) avoid the typical damaging corrosion phenomena of these electrodes. Indeed, ZnO-based photoanodes are susceptible to release Zn^{2+} ions when they stay in prolonged contact with acidic groups in the electrolyte/dye solution.[63,64] The dye loading time (abbreviated as x_1) and the molar ratio between CDCA and D131 in the ZnO-sensitizing solution (x_2) were chosen as factors, *i.e.*, the experimental variables of the DoE. This study was carried out for the DR morphology, and the results obtained were extended to the other typologies of ZnO samples investigated in this work.

The experimental domain was investigated with a composite face-centered (CCF) factorial design, a suitable model to identify the effects of interactions among factors on the measured responses, the latter being the photovoltaic performance figures of merit of the lab-scale prototypes (*i.e.*, J_{sc}, V_{oc}, FF, and PCE). In the CCF design, the experiments correspond to the vertices, the axial points, and the central point of a hypothetical square area that defines the explored experimental domain. In our study, each factor varied over three levels, *i.e.*, named as the minimum (−1), the central (0), and the maximum (+1). In particular, x_1 varied between 1 and 7 h, while x_2 changed between 18 and 50. The overall number of experiments was 22, including two replicas of each experimental condition and six replicas for the central point of the CCF design; these latter were used to check the model reproducibility.

Computational study

To gain insight into the behavior of different ZnO structures on the photoconversion efficiency, *ab initio* calculations were performed on the D131 dye molecule and the different surfaces exposed by ZnO. Since the calculations on the actual interface are too computationally demanding, the properties of interest of the dye and the particle surfaces (that is, the HOMO–LUMO gap and the absolute position of the band edges) were separately evaluated. From these properties, parameters connected to the electrochemical properties of the electrodes can be extracted to infer the origin of the experimental behavior of the different ZnO structures.

The dye structural and electronic properties were computed with density functional theory (DFT) and time-dependent-DFT (TD-DFT) calculations with the Gaussian16 program,[65] with a 6-311++G(d,p) Gaussian basis set at the B3LYP[66–68] and CAM-B3LYP[69] density functionals.

As regards investigation on ZnO structures, first-principles calculations were performed with the Vienna *ab initio* simulation package (VASP)[70,71] using Perdew, Burke, and Ernzherof (PBE)[72] density functional with a plane wave basis set with a kinetic energy cutoff of 600 eV; projected augmented wave pseudopotentials[73] were used to treat the core of the atoms. The reciprocal space was sampled with a *Γ*-centered 8 × 4 × 1 *k*-point mesh.

Results and discussion

Characterization of ZnO micro- and nanostructures

The crystallinity and purity grade of the synthetized particles was assessed by XRD (Fig. 1A). The sharp peaks of the XRD pattern can be ascribed to the single-crystalline phase of the wurtzite structure of ZnO. FESEM images demonstrate the

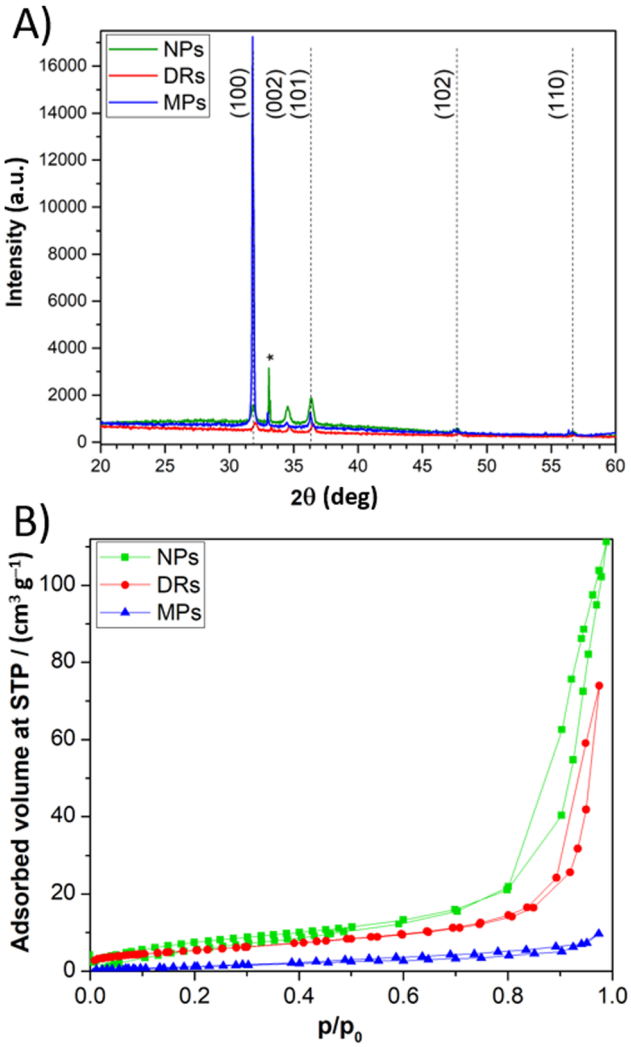

Fig. 1 (A) XRD pattern of the different ZnO microstructures: DRs (red line), MPs (blue line), and NPs (green line). (B) Nitrogen adsorption–desorption isotherms of different ZnO morphologies in powder form.

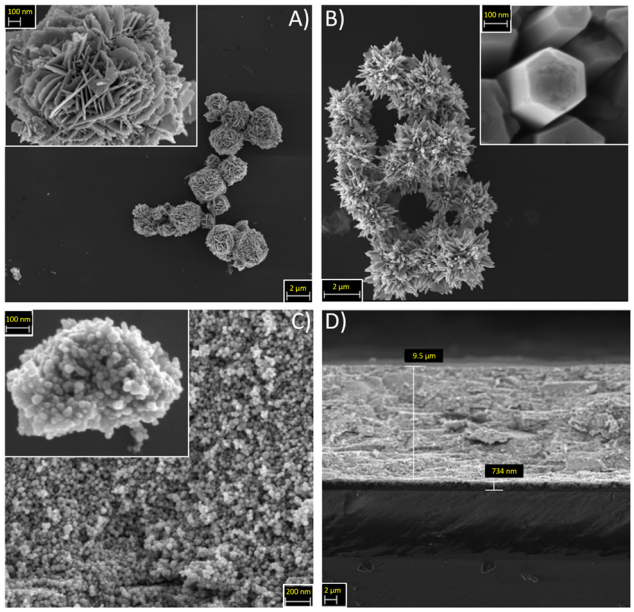

Fig. 2 FESEM images for different ZnO morphologies, namely (A) DRs, (B) MPs, and (C) NPs. (D) Cross-section image of a NPs-based photoanode.

excellent control of the morphology obtainable with the synthesis route adopted in this work (Fig. 2). In particular, it is evident that the peculiar nanostructuration of the particles depends on preparation conditions. First, DRs are flower-like aggregates with a diameter of about 2 µm, composed of 2D nanosheets with a uniform thickness of around 50 nm (Fig. 2A). Second, MPs consist of wires (diameter around 100 nm) with a hexagonal cross-section growth from a central point (Fig. 2B). Third, NPs of ≈20 nm diameters have a regular spherical shape and form aggregates with a diameter lower than 1 µm (Fig. 2C). The thickness of the ZnO layer on the FTO-covered glass was measured by cross-section FESEM images, and it was estimated to be about 9.5 µm (Fig. 2D).

Results of nitrogen adsorption–desorption measurements carried out on ZnO samples are shown in Fig. 1B. DRs and NPs are characterized by type IV isotherms, with a hysteresis loop in the pressure range of 0.8–0.95 p/p_0, indicative of mesopores, possibly due to interparticle porosities, with a diameter larger than 4 nm. On the contrary, a type III isotherm, typical of a non-porous material, was observed for MPs. The presence of porosity in DRs and NPs leads to a higher BET specific surface area (S_{BET}), equal to 19.59 and 29.64 $m^2\ g^{-1}$, respectively, much higher when compared to 5.22 $m^2\ g^{-1}$ of MPs sample.

Fig. S1 in the ESI† shows the UV-vis curves and band-gap values for the three ZnO morphologies.

Experimental and theoretical assessment of structure/performance correlation

The three ZnO morphologies were tested as photoanodes in aqueous DSSCs. Photovoltaic characterizations (Table 1) shows that the best performances were achieved in the presence of DRs. An interpretation of these solar cells results must be based on three fundamental criteria, namely the surface area of the electrode active material, the quantity of chemisorbed dye, and the interface among the particles constituting each electrode morphology.

MPs-based cells displayed a low photocurrent density due to a limited S_{BET}, responsible for insufficient dye loading. As far as DRs and NPs morphologies are concerned, the former was superior, in particular in terms of the photocurrent density of the corresponding solar cells. To investigate further, UV-VIS

Table 1 BET specific surface area for different ZnO morphologies, along with the photovoltaic parameters (measured under 1 sun irradiation, AM1.5G) of the corresponding aqueous DSSCs. *J*–*V* curves of representative cells for each morphology are shown in Fig. S2 in the ESI

Sample	S_{BET} [$m^2\ g^{-1}$]	J_{sc} [mA cm^{-2}]	V_{oc} [mV]	FF [%]	PCE [%]
DRs	19.59	1.75 ± 0.25	390 ± 58	51.1 ± 5.0	0.35 ± 0.04
NPs	29.64	1.09 ± 0.11	370 ± 10	51.8 ± 2.3	0.21 ± 0.02
MPs	5.22	0.54 ± 0.31	335 ± 20	47.6 ± 5.3	0.09 ± 0.06

spectroscopy was exploited to perform a comparative analysis of the amount of dye adsorbed by DRs- and NPs-based electrodes. A measurement of the dye concentration in the sensitizing solution before and after 1 h of dye loading was performed for each ZnO morphology. The dye concentration was calculated with the Lambert–Beer's law and a difference between the final and initial concentrations of −0.12 mM (−25%) and −0.21 mM (−44%) was found for DRs and NPs samples, respectively. This measure revealed that NPs could adsorb a greater amount of dye than DRs; this evidence was consistent with the higher value of BET specific surface area. However, the photovoltaic performance of DRs-based samples was better than that of the corresponding NPs-based devices. Here comes the importance of interfaces: even if NPs possessed higher S_{BET} and loaded dye molecules, they also counted a higher number of interfaces among adjacent particles, resulting in an ineffective (worse than that of DRs-based electrodes) electronic transfer through the whole electrode. In fact, 2D and interconnected nanosheets that form the DR microstructure facilitate the path for photoelectrons, thus providing faster electron transport and increasing the J_{sc}.[74] As regards nanostructures, the future activity of our team will be focused on morphologies able to offer a direct pathway for electron transport, *e.g.* nanotubes, that are known to improve the collection efficiency of the photoelectrode.[75]

Overall, DRs showed the best compromise between samples, ensuring at the same time a high specific surface area for dye adsorption and a suitable particle interconnection for electron transport.

Ab initio calculations on the D131 dye molecule and on the different surfaces exposed by ZnO were carried out to further investigate the behavior of DRs and NPs active materials when used in aqueous DSSCs. The dye minimum energy structure was optimized in acetonitrile and in methanol solvents, the former being the most common solvent in DSSCs, and the second the one in which the experimental adsorption spectrum was measured in this study. On these minima, a single point TD-DFT calculation was carried out to compute the vertical electronic transition energy, *i.e.*, the HOMO–LUMO gap. The calculated transition in methanol occurs at 414 nm, in good agreement with experimental data. Fig. 3A and B depicts the HOMO and LUMO molecular orbitals that are involved in this transition. While the HOMO is fully delocalized on the whole molecule, the LUMO involves the electron-acceptor moiety at the anchoring group. This favors the charge transfer process to the surface after photo-excitation of the dye.

As one can see from the XRD data (Fig. 1A), different morphologies expose different surfaces. DRs grow in the direction of the (0001) plane, exposing the $(10\bar{1}0)$ and $(10\bar{1}1)$ on the "surface of the petals", with the first being the dominant one. NPs, instead, show three different surfaces, namely $(10\bar{1}0)$, (0002), and $(10\bar{1}1)$, that have similar XRD intensities. Of the three surfaces above mentioned, only the first one is non-polar, with the other two exhibiting a strong dipole. Fig. 3C and D depicts the three surfaces as cut from bulk ZnO and a model surface slab that was used to calculate the electronic properties of one of these surfaces. From *ab initio* calculations we were able to obtain only the absolute position of the valence band

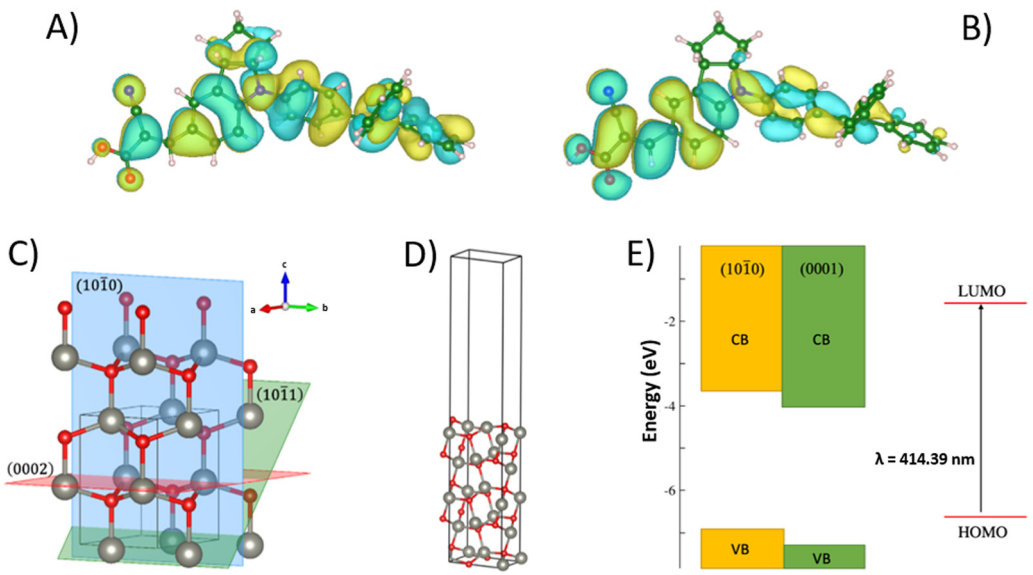

Fig. 3 (A) HOMO and (B) LUMO molecular orbitals of D131 dye in methanol solvent. Color code: carbon (green), hydrogen (light pink), oxygen (red), nitrogen (blue). Isosurface level = 1.16 × 10^{-2}; yellow and cyan refer to positive and negative values, respectively. (C) Lattice planes relevant to the morphologies under study. (D) 5-layer vacuum slab for the $(10\bar{1}0)$ surface. Colour code: zinc (grey), oxygen (red). (E) Energy diagram of ZnO bands relative to the position of the HOMO and LUMO levels of D131. The band edge positions of the $(10\bar{1}0)$ surface (yellow) are computed as described in the text. The positions of the (0001) surface bands edges (green) are calculated substracting the experimental work function variation to the values of the calculated band edges of the $(10\bar{1}0)$ surface.

edge of the non-polar $(10\bar{1}0)$ surface, and will reference to literature for the others.

First, ZnO bulk was optimized, then a 5-layer slab of the $(10\bar{1}0)$ surface with 15 Å of vacuum was built to avoid the interaction between the periodic images. After surface relaxation, the surface energy was computed, obtaining a value of 0.88 J m^{-2}, in agreement with literature results.[76] The absolute position of the valence band edge (the negative of the work-function) was assessed according to a computational protocol developed by Toroker *et al.*[77] as:

$$\text{Band edge} = \text{BGC}^{\text{Slab}} - E_{\text{vac}} \pm \frac{1}{2}E_{\text{gap}}$$

where the bandgap center BGC^{Slab} is the energy average of the highest occupied and lowest unoccupied states of the slab model as obtained from DFT calculations, E_{vac} is the converged energy at the vacuum region as obtained for the computed averaged electrostatic potential, and E_{gap} refers to the bandgap of bulk ZnO. In this case, we adopted the experimental E_{gap} value,[78] since standard DFT generalized gradient approximation functionals as PBE are known to underestimate band gaps of semiconductors. On the polar surfaces, the band edge positions are defined within this model, since the strong dipole corrections affect the vacuum energy. Thus, to evaluate the position of the (0001) surface, we referred to the experimental measurement of the work function shift reported by Moorman *et al.*[79] and used this value to shift the calculated band edge of the other surface.

Fig. 3E depicts the energy level diagram for the $(10\bar{1}0)$ and (0001) surfaces together with the position of the D131 frontier orbitals. From these data, a higher driving force for electron injection from the D131 LUMO to the conduction band can be predicted for the (0001) surface with respect to the $(10\bar{1}0)$ one. On the other hand, the absolute position of the conduction band edge gives us information about the V_{oc} of the cell, that is defined as the difference between this value and the redox potential of the electrolyte couple. The lower the band edge, the lower the V_{oc}. If we take the $(10\bar{1}0)$ surface as being representative of the DRs morphology, since it is by far the most abundant exposed surface, we can consider the (0001) surface as indicative of the behavior of the NPs, in which this surface is present together with the former. The lower position of the (0001) conduction band well agrees with the lower V_{oc} measured for the NPs with respect to the DRs.

Table 2 Experimental matrix for the CCF DoE, where x_1 is the dye loading time and x_2 is the molar ratio between CDCA and D131 in the ZnO-sensitizing solution. The corresponding experimental responses, *i.e.* the photovoltaic performance of the lab-scale aqueous DSSCs under 1 sun irradiation (AM1.5G), are also given

Experiment	x_1 [h]	x_2	J_{sc} [mA cm^{-2}]	V_{oc} [mV]	FF [%]	PCE [%]
F1	1 (−1)	18 (−1)	1.42	319	44.5	0.20
F2	1 (−1)	18 (−1)	1.80	318	47.3	0.27
F3	1 (−1)	34 (0)	1.58	348	44.4	0.24
F4	1 (−1)	34 (0)	1.70	351	45.1	0.27
F5	1 (−1)	50 (+1)	1.83	329	45.9	0.28
F6	1 (−1)	50 (+1)	2.01	340	49.1	0.35
F7	4 (0)	18 (−1)	1.22	357	45.2	0.19
F8	4 (0)	18 (−1)	0.85	304	30.0	0.08
F9	4 (0)	34 (0)	1.72	339	40.5	0.24
F10	4 (0)	34 (0)	1.67	360	42.9	0.26
F11	4 (0)	34 (0)	2.10	343	45.4	0.33
F12	4 (0)	34 (0)	1.60	345	47.0	0.26
F13	4 (0)	34 (0)	1.76	337	48.3	0.29
F14	4 (0)	34 (0)	1.57	360	46.2	0.26
F15	4 (0)	50 (+1)	2.03	331	48.3	0.32
F16	4 (0)	50 (+1)	1.86	344	38.5	0.25
F17	7 (+1)	18 (−1)	1.24	328	42.1	0.17
F18	7 (+1)	18 (−1)	1.34	234	27.6	0.09
F19	7 (+1)	34 (0)	1.79	344	44.9	0.28
F20	7 (+1)	34 (0)	1.97	325	48.1	0.31
F21	7 (+1)	50 (+1)	1.42	356	46.1	0.23
F22	7 (+1)	50 (+1)	1.44	357	47.9	0.25

Chemometric investigation of photovoltaic performances

The optimization of the sensitization procedure was carried out for the most efficient ZnO morphology, *i.e.* the DRs, using a CCF DoE. The role of each of the experimental parameters and their mutual interactions influencing the photovoltaic performances (*i.e.*, J_{sc}, V_{oc}, FF, PCE) of lab-scale DSSCs were evaluated with MODDE software. Table 2 shows the experimental matrix with all the aqueous DSSCs assembled and tested to investigate the whole experimental domain. In detail, each trial was repeated twice, including the three replicas of the central point. The latter, which numerically corresponds to the intermediate value for each variable, is crucial to assess the experimental reproducibility. The collected data showed a good reproducibility of the measured quantities for DSSCs prepared in the same conditions.

Data from the DoE analysis show average efficiency values ranging between 0.13 and 0.35%. The worst efficiency was obtained for the sensitization condition corresponding to 7 h of dipping time and a D131/CDCA molar ratio equal to 18. On the contrary, the maximum efficiency was reached for the shortest immersion time (1 h) and for a molar ratio between D131 and CDCA equal to 1 : 50. The efficiencies obtained with ZnO-based anode and water-based electrolyte are close to our previous results on untreated TiO_2 nanoparticles.[80]

According to the CCF model, a certain experimental response can be expressed accordingly to eqn (1):

$$y = b_0 + b_1x_1 + b_2x_2 + b_{11}{x_1}^2 + b_{22}{x_2}^2 + b_{12}x_1x_2 \quad (1)$$

where x_1 and x_2 represent the experimental variables, while b_0, b_1, ... are the coefficients that describe the reciprocal interaction between factors and responses. The values of such coefficients, which quantify the importance of each factor in the equation, can be extrapolated by the model using the software MODDE. The following equations were obtained for each figure of merit obtained from *J–V* measurements:

$$J_{\text{sc}} = 1.716 - 0.077x_1 + 0.176x_2 + 0.026{x_1}^2 - 0.113{x_2}^2 - 0.022x_1x_2 \quad (2)$$

$$V_{\text{oc}} = 348.6 - 4.4x_1 + 12.1x_2 - 4.7{x_1}^2 - 9.6{x_2}^2 + 8.6x_1x_2 \quad (3)$$

$$\text{FF} = 45.9 - 1.0x_1 + 2.4x_2 - 0.3{x_1}^2 - 1.8{x_2}^2 + 0.8x_1x_2 \quad (4)$$

$$\mathrm{PCE} = 0.272 - 0.018x_1 + 0.042x_2 + 0.001{x_1}^2 - 0.029{x_2}^2 + 0.003x_1x_2 \quad (5)$$

Isoresponse surfaces were drawn to visually evaluate how the aqueous DSSCs performance depended on the investigated parameters; these surfaces are also helpful in predicting the value of each photovoltaic parameter as a function of the investigated factors (Fig. 4). In particular, it was observed that the photovoltaic performance of a ZnO-based aqueous DSSC improved when the immersion time was minimized and the concentration of CDCA in the sensitizing solution increased. In detail, the increase in the amount of CDCA proved to be beneficial for all the photovoltaic parameters, especially for high immersion times, as usually observed with TiO_2-based photoanodes.[81] One of CDCA main roles is to promote the formation of a dye monolayer onto the electrode surface. The co-adsorbants are believed to compete with the dye molecules in the first chemisorption step, thus suppressing the formation of adsorption sites originating from two adjacent dye molecules. In this way, the realization of an overlying layer is avoided. Moreover, the CDCA prevents the formation of dye aggregates, which behave like deep traps that catalyse the photoelectron recombination with I_3^- ions present in the electrolyte.[82] In contrast, the increase in the sensitization time is detrimental. First, after the complete saturation of the available sites, the excess of dye molecules cannot be adsorbed directly onto the photoelectrode surface and, thus, are not useful for the injection process.[75] In addition, when CDCA is present at too low concentration values to counteract the aggregation of the dye and the multilayer formation, these detrimental phenomena occur, causing a reduction in the electron injection efficiency and, hence, on the overall cell performance.

EIS measurements were performed on aqueous DSSCs with particular attention on those devices based on photoanodes prepared under different experimental conditions. In detail, here we report cells corresponding to the vertices of the CCF DoE matrix. A representative Nyquist's plot is reported in Fig. 5A, referring to an aqueous DSSC prepared under optimal conditions. The impedance data were analysed using a suitable equivalent electrical circuit (inset in Fig. 5A). In particular, the charge-transfer resistance (R_{ct}) at the ZnO/dye/electrolyte interface is a measure of the recombination phenomena occurring between the electrons injected in the conduction band of the

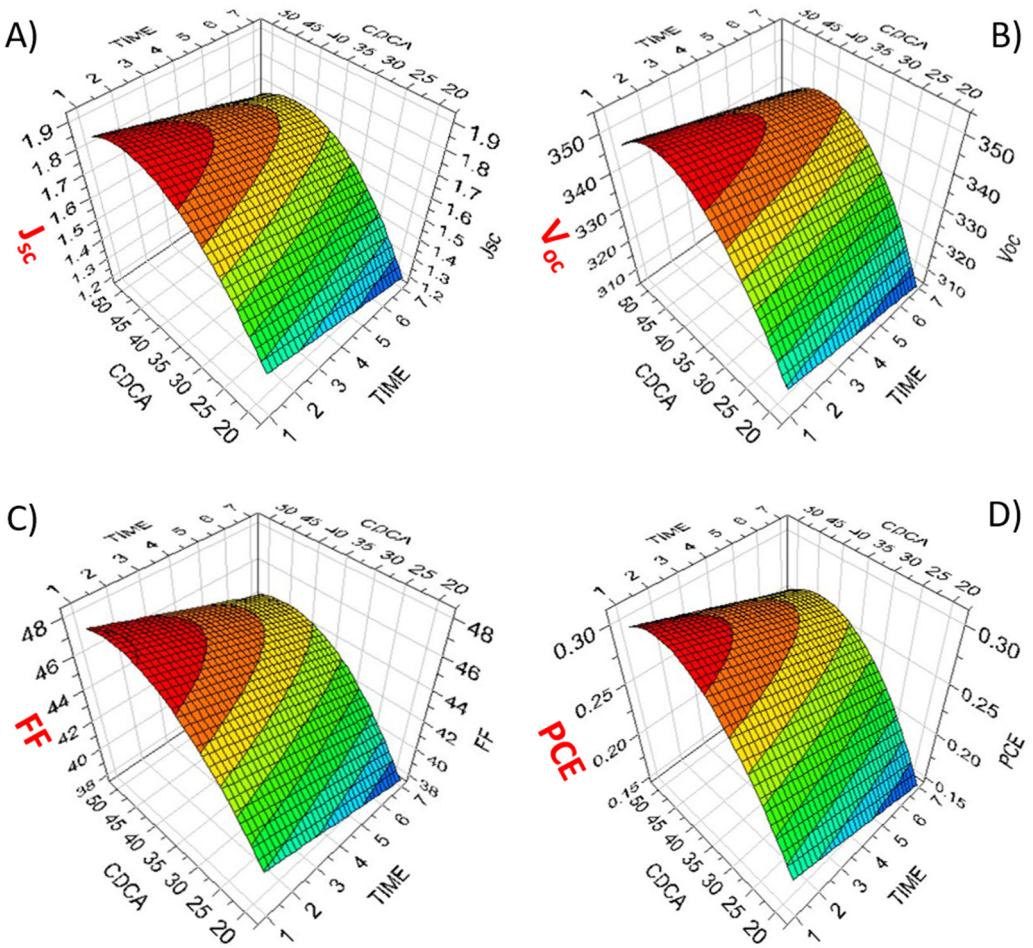

Fig. 4 Isoresponse surfaces show the effect of dye loading time (label: TIME) and CDCA:dye molar ratio (label : CDCA) on the photovoltaic parameters of aqueous DSSCs: (A) J_{sc}, (B) V_{oc}, (C) FF, (D) PCE.

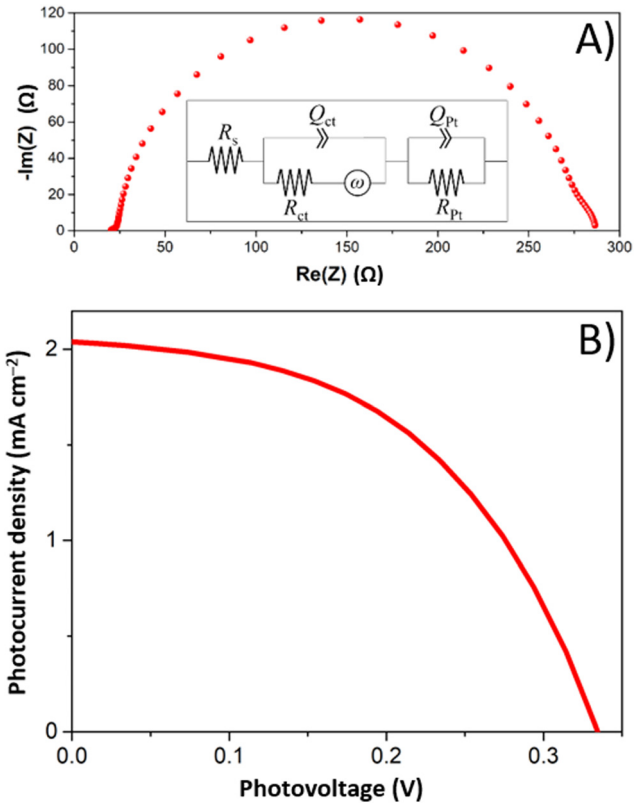

Fig. 5 (A) Nyquist plot of a ZnO-based aqueous DSSC. Inset: Equivalent electric circuit used for data fitting, based on series resistance (R_s), constant phase element (Q_{ct}), and charge transfer resistance (R_{ct}) at the ZnO/dye/electrolyte interface, diffusion resistance (ω) of the redox couple, constant phase element (Q_{Pt}), and charge transfer resistance (R_{Pt}) at the Pt/electrolyte interface. (B) J–V curve measured under 1 sun irradiation (AM1.5G) for a ZnO-based aqueous DSSC prepared following the optimized sensitizing conditions for photoanode fabrication, *i.e.*, 1 h of dye loading time and molar ratio = 1 : 50 between dye and CDCA.

semiconductor and the I_3^- ions of the electrolyte; this parameter is among the most important when photoanodes are investigated. The EIS analysis revealed the increase of R_{ct} values as long as the dipping time was reduced and the concentration of CDCA was increased at low dipping times. These data agree with the evidence come out from the photovoltaic measurements previously discussed. The combined results of the EIS and J–V measurements are summarized in Table 3.

In detail, keeping the dipping time constant at 1 h, the value of R_{ct} raised as the CDCA concentration increased. This effect seems to confirm the limitation of the recombination reactions in the presence of this additive, also resulting in increased V_{oc} values. On the contrary, increasing the dipping time favors the formation of aggregates or multilayers on the photoanode surface. This event is detrimental to the electron injection processes – as previously mentioned – because aggregated dye molecules tend to reciprocally quench any excited state formed under sunlight. Moreover, only dye molecules chemically bond to the semiconductor surface can inject electrons in the conduction band of the ZnO electrode. In fact, the non-chemisorbed ones not only cannot participate in the injection

Table 3 Results of EIS and J–V measurements on DSSCs prepared in the experimental conditions corresponding to the vertices of the CCF-DoE domain

x_1 [h]	x_2	R_{ct} [Ohm]	J_{sc} [mA cm^{-2}]	V_{oc} [mV]	FF [%]	PCE [%]
1	18	92	1.80	318	47.3	0.27
1	50	116	2.01	340	49.1	0.35
7	18	84	1.24	328	42.1	0.17
7	50	70	1.42	356	46.1	0.23

process, but they also act as a filter of the solar light for the underlying layers. Given these premises, it is intuitive to think that a more prolonged electrode immersion in the dye solution leads to a more pronounced dissolution/etching of ZnO.

The results obtained from the DoE and the EIS measurements suggested moving toward further reductions of the dipping time. In order to check this possibility, the halving of the dipping time (up to 30 min) was tried. However, a reduction of the average efficiency from 0.34 to 0.30% was experienced for two cell batches, probably due to the insufficient dipping time, which causes low light harvesting efficiency.[82] Therefore, it can be stated that the best sensitization conditions for the examined system are represented by 1 h of immersion time and a dye solution characterized by a molar ratio of 1 : 50 between dye and CDCA. The J–V curve obtained in the optimized sensitizing conditions is illustrated in Fig. 5B.

Long-term stability of lab-scale ZnO-based aqueous DSSCs

The stability of DSSCs prepared under optimized conditions was assessed by means of J–V measurements over time. Monitoring was performed for the two most efficient photoanode families, *i.e.*, DRs and NPs, and the corresponding solar cells were stored under dark and at room temperature. The photovoltaic parameters, normalized to the values measured immediately after cells assembly, are reported as a function of time in Fig. 6. The general trend for both microstructures was a preservation of the initial value of each figure of merit over the measurement period (*i.e.*, more than 4 months). In addition, the increase in current density (and consequently in the overall cell efficiency) is worth noting during the first two months for both ZnO-based devices. We already detected this situation[83] when working with aqueous electrolytes containing a low amount of Na-CMC (up to 4.5 wt%). In the present work, NPs-based photoanodes showed a more significant improvement of photovoltaic parameters over time than DRs-based cells. The mesoporous layer made of NPs is likely more compact since it comprises smaller particles. Therefore, its filling by the electrolyte and the subsequent achievement of the maximum efficiency require a longer period of time.

Overall, both the devices were able to keep – after more than 4 months – an efficiency higher than that measured just after cell assembly, and this is truly outstanding, also justifying the current research efforts by the scientific community in the aqueous DSSCs field.[84,85]

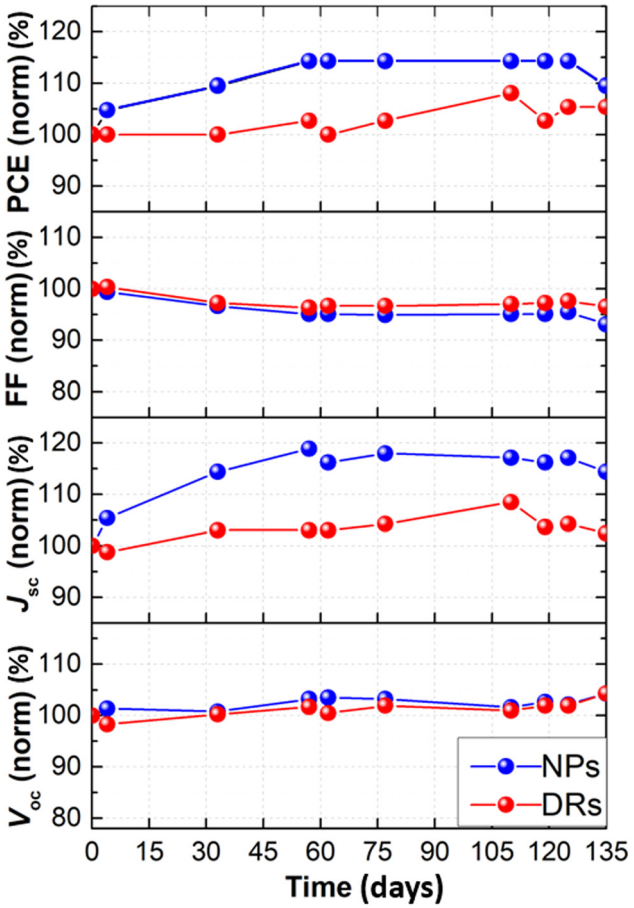

Fig. 6 Normalized photovoltaic parameters *versus* time for aqueous DSSCs prepared with DRs- and NPs-based photoanodes, stored under dark conditions and ambient temperature.

Conclusions

Three ZnO morphologies (*i.e.*, NPs, DRs, MPs) were investigated to prepare photoelectrodes for aqueous DSSCs. After assessing each of their morphology, structure, and surface area, ZnO samples were sensitized with D131 molecular dye, and the photovoltaic performances of the resulting aqueous DSSCs were measured. DRs led to the most efficient solar cells due to their compromise in terms of high specific surface area for dye adsorption and suitable particle interconnection for electron transport. From theoretical calculations, the better performance of DRs-based cells was also attributed to the more suitable alignment between the energy level of the exposed ZnO surfaces and the position of the D131 frontier orbitals. A DoE approach was set up to optimize the sensitization conditions of the DRs electrodes regarding dye concentration, presence of the co-adsorbent agent, and immersion time. This led to efficiency values reaching 0.35%, which increased upon time when cells were subjected to a stability test carried out for more than four months. Even if the achieved efficiency is still low if compared with other state-of-art aqueous DSSCs studies present in the literature, the present findings have demonstrated for the first time that ZnO can be used for these water-based photovoltaic cells and future studies, mainly aimed at exploring new morphologies or surface treatments, could lead to a tangible boosting of the solar-to-electricity conversion performances.

Author contributions

F. B.: conceptualization, writing – original draft, funding acquisition. E. M.: investigation, writing – original draft. S. G., E. S., N. G., A. Y. S. Z.: investigation, data curation. A. B. M. G., M. P., C. G.: methodology, formal analysis. C. B.: supervision, funding acquisition. V. C.: conceptualization, methodology.

Conflicts of interest

There are no conflicts to declare.

Acknowledgements

This project has received funding from the European Research Council (ERC) under the European Union's Horizon 2020 research and innovation programme (grant agreement no. 948769, project title: SuN_2rise). A PhosAgro/UNESCO/IUPAC research grant in green chemistry has supported this research. C. B. and S. G. acknowledge support from the Project CH4.0 under the MUR program "Dipartimenti di Eccellenza 2023-2027" (CUP D13C22003520001). S. G. acknowledges support from project NODES, which has received fundings from the MUR-M4C2 1.5 of PNRR funded by the European Union - NextGenerationEU (grant agreement no. ECS00000036).

References

1 A. V. Komarova, I. V. Filimonova and A. A. Kartashevich, *Energy Rep.*, 2022, **8**, 683–690.
2 I. Campos, M. Brito, D. De Souza, A. Santino, G. Luz and D. Pera, *J. Cleaner Prod.*, 2022, **365**, 132763.
3 K. Pan, F. Wang, S. Wei, S. H. Siyal, Y. Ren, L. Xu, X. Wu and Q. Li, *Compos. Commun.*, 2020, **19**, 82–89.
4 M. A. Cardoso, S. F. H. Correia, A. R. Frias, H. M. R. Gonçalves, R. F. P. Pereira, S. C. Nunes, M. Armand, P. S. André, V. de Zea Bermudez and R. A. S. Ferreira, *J. Rare Earths*, 2020, **38**, 531–538.
5 Y. Liu and L. Guo, *J. Chem. Phys.*, 2020, **152**, 100901.
6 A. Caragliu and M. Graziano, *Energy Policy*, 2022, **168**, 113154.
7 D. Borozan, *Renewable Sustainable Energy Rev.*, 2022, **165**, 112621.
8 M. Z. Akgul, A. Figueroba, S. Pradhan, Y. Bi and G. Konstantatos, *ACS Photonics*, 2020, **7**, 588–595.
9 A. K. Mishra, R. Belgamwar, R. Jana, A. Datta and V. Polshettiwar, *Proc. Natl. Acad. Sci. U. S. A.*, 2020, **117**, 6383–6390.
10 X. Dai, K. Xu and F. Wei, *Beilstein J. Nanotechnol.*, 2020, **11**, 51–60.

11 D. Peñaloza, É. Mata, N. Fransson, H. Fridén, Á. Samperio, A. Quijano and A. Cuneo, *Renewable Sustainable Energy Rev.*, 2022, **155**, 111867.
12 T. Huld, E. Salis, A. Pozza, W. Herrmann and H. Müllejans, *Sol. Energy*, 2016, **133**, 349–362.
13 D. J. Xue, Y. Hou, S. C. Liu, M. Wei, B. Chen, Z. Huang, Z. Li, B. Sun, A. H. Proppe, Y. Dong, M. I. Saidaminov, S. O. Kelley, J. S. Hu and E. H. Sargent, *Nat. Commun.*, 2020, **11**, 1514.
14 L. Li, *Nanomaterials*, 2020, **10**, 559.
15 Y. F. Makableh, I. Abu Awad, W. Hassan and G. Aljaiuossi, *Sol. Energy*, 2020, **202**, 204–209.
16 V. Benda and L. Černá, *Heliyon*, 2020, **6**, e05666.
17 N. S. M. N. Izam, Z. Itam, W. L. Sing and A. Syamsir, *Energies*, 2022, **15**, 2790.
18 M. Victoria, N. Haegel, I. M. Peters, R. Sinton, A. Jäger-Waldau, C. del Cañizo, C. Breyer, M. Stocks, A. Blakers, I. Kaizuka, K. Komoto and A. Smets, *Joule*, 2021, **5**, 1041–1056.
19 S. Mishra, S. Ghosh, B. Boro, D. Kumar, S. Porwal, M. Paul, H. Dixit and T. Singh, *Energy Adv.*, 2022, **1**, 761–792.
20 F. Rehman, I. H. Syed, S. Khanam, S. Ijaz, H. Mehmood, M. Zubair, Y. Massoud and M. Q. Mehmood, *Energy Adv.*, 2023, **2**, 1239–1262.
21 M. M. Tavakoli, D. Prochowicz, P. Yadav and R. Tavakoli, *Phys. Status Solidi RRL*, 2020, **14**, 2000062.
22 Z. Niu, T. Lei, H. Dong, Z. Deng, W. Zhao, F. Li, S. Ye and Z. Wu, *Org. Electron.*, 2020, **82**, 105710.
23 R. J. Stoddard, W. A. Dunlap-Shohl, H. Qiao, Y. Meng, W. F. Kau and H. W. Hillhouse, *ACS Energy Lett.*, 2020, **5**, 946–954.
24 Q. Yang, R. Dettori, G. Yuan and L. R. Anderson, *Sol. Energy*, 2020, **201**, 541–546.
25 Y. Mo, C. Wang, X. Zheng, P. Zhou, J. Li, X. Yu, K. Yang, X. Deng, H. Park, F. Huang and Y. Cheng, *Interdiscip. Mater.*, 2022, **1**, 309–315.
26 W. Tian, P. Song, Y. Zhao, L. Shen, K. Liu, L. Zheng, Y. Luo, C. Tian, L. Xie and Z. Wei, *Interdiscip. Mater.*, 2022, **1**, 526–536.
27 C. Lin, Y. Liu, G. Wang, K. Li, H. Xu, W. Zhang, C. Shao and Z. Yang, *ACS Omega*, 2021, **6**, 715–722.
28 C. Lin, Y. Liu, D. Shao, G. Wang, H. Xu, C. Shao, W. Zhang and Z. Yang, *RSC Adv.*, 2021, **11**, 3071–3078.
29 C. L. Castro-Riquelme, A. Ochoa-Terán, J. C. Calva-Yáñez, E. A. Reynoso-Soto and R. M. Félix-Navarro, *Mater. Renewable Sustainable Energy*, 2021, **10**, 2.
30 P. Mariani, A. Agresti, L. Vesce, S. Pescetelli, A. L. Palma, F. Tomarchio, P. Karagiannidis, A. C. Ferrari and A. Di Carlo, *ACS Appl. Energy Mater.*, 2021, **4**, 98–110.
31 A. U. Rehman, M. Khan, A. D. Khan, A. A. Raja, M. Aslam, S. Khan and M. Imran, *Jpn. J. Appl. Phys.*, 2021, **60**, 011004.
32 R. K. Kothandaraman, Y. Jiang, T. Feurer, A. N. Tiwari and F. Fu, *Small Methods*, 2020, **4**, 2000395.
33 J. Zhou, Q. Huang, Y. Ding, G. Hou and Y. Zhao, *Nano Energy*, 2022, **92**, 106712.
34 M. I. Elsmani, N. Fatima, M. P. A. Jallorina, S. Sepeai, M. S. Su'ait, N. A. Ludin, M. A. M. Teridi, K. Sopian and M. A. Ibrahim, *Nanomaterials*, 2021, **11**, 3186.
35 F. Grifoni, M. Bonomo, W. Naim, N. Barbero, T. Alnasser, I. Dzeba, M. Giordano, A. Tsaturyan, M. Urbani, T. Torres, C. Barolo and F. Sauvage, *Adv. Energy Mater.*, 2021, **11**, 2101598.
36 N. M. Saidi, N. K. Farhana, S. Ramesh and K. Ramesh, *Sol. Energy*, 2021, **216**, 111–119.
37 A. B. Muñoz-García, I. Benesperi, G. Boschloo, J. J. Concepcion, J. H. Delcamp, E. A. Gibson, G. J. Meyer, M. Pavone, H. Pettersson, A. Hagfeldt and M. Freitag, *Chem. Soc. Rev.*, 2021, **50**, 12450–12550.
38 K. Devulapally, G. Reddy, S. Prasanthkumar, A. Jagadeesh, S. Soman and L. Giribabu, *J. Porphyrins phthalocyanines*, 2021, **25**, 407–417.
39 V. V. Divya and C. H. Suresh, *New J. Chem.*, 2021, **45**, 2496–2507.
40 F. Bella, C. Gerbaldi, C. Barolo and M. Grätzel, *Chem. Soc. Rev.*, 2015, **44**, 3431–3473.
41 A. Romero-Contreras, J. S. Lezama Pacheco, J. Alvarado, U. Pal and J. Villanueva-Cab, *ACS Appl. Energy Mater.*, 2022, **5**, 4817–4828.
42 J. H. Kim, D. H. Kim, J. H. So and H. J. Koo, *Energies*, 2022, **15**, 219.
43 C. T. Li, R. Y. Y. Lin and J. T. Lin, *Chem. – Asian J.*, 2017, **12**, 486–496.
44 B. Karuppasamy, B. Shenbagabalakrishnan and V. Gayathri, *Sol. Energy*, 2022, **236**, 608–612.
45 B. Selvaraj, G. Shanmugam, S. Kamaraj, E. Thirugnanasambandam, A. Gunasekeran and A. Sambandam, *Sol. Energy*, 2022, **236**, 586–598.
46 M. Jilakian and T. H. Ghaddar, *ACS Appl. Energy Mater.*, 2022, **5**, 257–265.
47 J. C. De Haro, E. Tatsi, L. Fagiolari, M. Bonomo, C. Barolo, S. Turri, F. Bella and G. Griffini, *ACS Sustainable Chem. Eng.*, 2021, **9**, 8550–8560.
48 D. Albulescu, D. Ursu, L. M. Rusnac, S. Nitu, M. Miclau and M. Vajda, *Crystals*, 2022, **12**, 98.
49 A. K. Singh and J. Nithyanandhan, *ACS Appl. Energy Mater.*, 2021, **4**, 13932–13942.
50 H. Shahroosvand, L. Heydari, S. Tarighi, M. Riahi, B. N. Bideh and B. Pashaei, *Int. J. Hydrogen Energy*, 2017, **42**, 16421–16427.
51 B. Pham, D. Willinger, N. K. McMillan, J. Roye, W. Burnett, A. D'Achille, J. L. Coffer and B. D. Sherman, *Sol. Energy*, 2021, **224**, 984–991.
52 S. Husmann, L. F. Lima, L. S. Roman and A. J. G. Zarbin, *ChemSusChem*, 2018, **11**, 1238–1245.
53 L. Fagiolari, M. Bonomo, A. Cognetti, G. Meligrana, C. Gerbaldi, C. Barolo and F. Bella, *ChemSusChem*, 2020, **13**, 6562–6573.
54 R. K. Kokal, S. Bhattacharya, L. S. Cardoso, P. B. Miranda, V. R. Soma, P. Chetti, D. Melepurath and S. S. K. Raavi, *Sol. Energy*, 2019, **188**, 913–923.
55 H. Ellis, R. Jiang, S. Ye, A. Hagfeldt and G. Boschloo, *Phys. Chem. Chem. Phys.*, 2016, **18**, 8419–8427.
56 F. Bella, L. Porcarelli, D. Mantione, C. Gerbaldi, C. Barolo, M. Grätzel and D. Mecerreyes, *Chem. Sci.*, 2020, **11**, 1485–1493.

57 R. Y. Y. Lin, F. L. Wu, C. T. Li, P. Y. Chen, K. C. Ho and J. T. Lin, *ChemSusChem*, 2015, **8**, 2503–2513.
58 J. Mizuno, M. Jeem, Y. Takahashi, M. Kawamoto, K. Asakura and S. Watanabe, *ACS Appl. Nano Mater.*, 2020, **3**, 1783–1791.
59 A. M. Tantray and M. A. Shah, *Chem. Pap.*, 2021, **75**, 1739–1747.
60 D. Kumar, *Eng. Res. Express*, 2021, **3**, 042004.
61 R. Kumar, A. Umar, G. Kumar, H. S. Nalwa, A. Kumar and M. S. Akhtar, *J. Mater. Sci.*, 2017, **52**, 4743–4795.
62 R. Vittal and K. C. Ho, *Renewable Sustainable Energy Rev.*, 2017, **70**, 920–935.
63 B. Onwona-Agyeman, M. Nakao, G. R. A. Kumara, S. M. M. L. Karunarathne, S. G. Anuradha and N. Dematage, *Prog. Photovoltaics Res. Appl.*, 2014, **22**, 661–665.
64 N. Shahzad, D. Pugliese, V. Cauda, M. I. Shahzad, Z. Shah, M. A. Baig and E. Tresso, *J. Photochem. Photobiol., A*, 2017, **337**, 192–197.
65 M. J. Frisch, G. W. Trucks, H. B. Schlegel, G. E. Scuseria, M. A. Robb, J. R. Cheeseman, G. Scalmani, V. Barone, G. A. Petersson, H. Nakatsuji, X. Li, M. Caricato, A. V. Marenich, J. Bloino, B. G. Janesko, R. Gomperts, B. Mennucci, H. P. Hratchian, J. V. Ortiz, A. F. Izmaylov, J. L. Sonnenberg, D. Williams-Young, F. Ding, F. Lipparini, F. Egidi, J. Goings, B. Peng, A. Petrone, T. Henderson, D. Ranasinghe, V. G. Zakrzewski, J. Gao, N. Rega, G. Zheng, W. Liang, M. Hada, M. Ehara, K. Toyota, R. Fukuda, J. Hasegawa, M. Ishida, T. Nakajima, Y. Honda, O. Kitao, H. Nakai, T. Vreven, K. Throssell, J. A. Montgomery Jr., J. E. Peralta, F. Ogliaro, M. J. Bearpark, J. J. Heyd, E. N. Brothers, K. N. Kudin, V. N. Staroverov, T. A. Keith, R. Kobayashi, J. Normand, K. Raghavachari, A. P. Rendell, J. C. Burant, S. S. Iyengar, J. Tomasi, M. Cossi, J. M. Millam, M. Klene, C. Adamo, R. Cammi, J. W. Ochterski, R. L. Martin, K. Morokuma, O. Farkas, J. B. Foresman and D. J. Fox, *Gaussian 16, Revision A.02*, Gaussian, Inc., Wallingford CT, 2016.
66 A. D. Becke, *J. Chem. Phys.*, 1993, **98**, 5648–5652.
67 C. Lee, W. Yang and R. G. Parr, *Phys. Rev. B: Condens. Matter Mater. Phys.*, 1988, **37**, 785–789.
68 P. J. Stephens, F. J. Devlin, C. F. Chabalowski and M. J. Frisch, *J. Chem. Phys.*, 1994, **98**, 11623–11627.
69 T. Yanai, D. P. Tew and N. C. Handy, *Chem. Phys. Lett.*, 2004, **393**, 51–57.
70 G. Kresse and J. Furthmüller, *Comput. Mater. Sci.*, 1996, **6**, 15–50.
71 G. Kresse and J. Furthmüller, *Phys. Rev. B: Condens. Matter Mater. Phys.*, 1996, **54**, 11169–11186.
72 J. P. Perdew, K. Burke and M. Ernzerhof, *Phys. Rev. Lett.*, 1996, **77**, 3865–3868.
73 P. E. Blöchl, *Phys. Rev. B: Condens. Matter Mater. Phys.*, 1994, **50**, 17953–17979.
74 A. Omar and A. Abdullah, *Renewable Sustainable Energy Rev.*, 2014, **31**, 149–157.
75 H. M. Cheng, W. H. Chiu, C. H. Lee, S. Y. Tsai and W. F. Hsieh, *J. Phys. Chem. C*, 2008, **112**, 16359–16364.
76 D. Mora-Fonz, J. Buckeridge, A. J. Logsdail, D. O. Scanlon, A. A. Sokol, S. Woodley and C. R. A. Catlow, *J. Phys. Chem. C*, 2015, **119**, 11598–11611.
77 M. C. Toroker, D. K. Kanan, N. Alidoust, L. Y. Isseroff, P. Liao and E. A. Carter, *Phys. Chem. Chem. Phys.*, 2011, **13**, 16644–16654.
78 V. Srikant and D. R. Clarke, *J. Appl. Phys.*, 1998, **83**, 5447–5451.
79 H. Moormann, D. Kohl and G. Heiland, *Surf. Sci.*, 1979, **80**, 261–264.
80 M. Bonomo, A. Y. Segura Zarate, L. Fagiolari, A. Damin, S. Galliano, C. Gerbaldi, F. Bella and C. Barolo, *Mater. Today Sustainability*, 2023, **21**, 100271.
81 S. Galliano, F. Bella, M. Bonomo, G. Viscardi, C. Gerbaldi, G. Boschloo and C. Barolo, *Nanomaterials*, 2020, **10**, 1585.
82 Y. Sakuragi, X. F. Wang, H. Miura, M. Matsui and T. Yoshida, *J. Photochem. Photobiol., A*, 2010, **216**, 1–7.
83 F. Bella, S. Galliano, M. Falco, G. Viscardi, C. Barolo, M. Grätzel and C. Gerbaldi, *Green Chem.*, 2017, **19**, 1043–1051.
84 M. Ö. Karakuş, M. E. Yakışıklıer, A. Delibaş and H. Çetin, *Electrochim. Acta*, 2022, **427**, 140841.
85 N. Sangiorgi, A. Sangiorgi and A. Sanson, *J. Electroanal. Chem.*, 2022, **915**, 116352.